INTERNATIONAL JOURNAL FOR NUMERICAL METHODS IN FLUIDS
Int. J. Numer. Meth. Fluids 2000; **34**: 279–305

A finite element thermally coupled flow formulation for phase-change problems

Marcela A. Cruchaga* and Diego J. Celentano

Departamento de Ingeniería Mecánica, Universidad de Santiago de Chile, Avda. Bdo. O'Higgins 3363, Santiago de Chile, Chile

SUMMARY

A finite element, thermally coupled incompressible flow formulation considering phase-change effects is presented. This formulation accounts for natural convection, temperature-dependent material properties and isothermal and non-isothermal phase-change models. In this context, the full Navier–Stokes equations are solved using a generalized streamline operator (GSO) technique. The highly non-linear phase-change effects are treated with a temperature-based algorithm, which provides stability and convergence of the numerical solution. The Boussinesq approximation is used in order to consider the temperature-dependent density variation. Furthermore, the numerical solution of the coupled problem is approached with a staggered incremental-iterative solution scheme, such that the convergence criteria are written in terms of the residual vectors. Finally, this formulation is used for the solutions of solidification and melting problems validating some numerical results with other existing solutions obtained with different methodologies. Copyright © 2000 John Wiley & Sons, Ltd.

KEY WORDS: natural convection; phase-change; thermally coupled flows

1. INTRODUCTION

Thermally coupled flows including phase-change effects are often encountered in several engineering applications of interest, such as in the metals processing industry and in energy storage systems. The energy transport or advective effect in these problems is important because heat transfer during the process can determine the overall efficiency and evolution of it. Moreover, the coupling between the mechanical and thermal behaviours of the fluid may also be due to density gradients caused by temperature variations (the flow motion is originated by buoyancy forces), the dissipation of mechanical work into heat in highly viscous flows and, finally, the phase-change phenomenon, which may strongly change the flow pattern. In the isothermal phase-change case, the location of the liquid–solid interface moves in time,

* Correspondence to: Departamento de Ingeniería Mecánica, Universidad de Santiago de Chile, Avda. Bdo. O'Higgins 3363, Santiago de Chile, Chile.

Received September 1998
Revised February 1999

resulting in a variable liquid domain. Further, for the non-isothermal phase-change case, the flow behaviour in the variable mushy and liquid phases is different due to the development of resistance to flow in the mushy region. In fact, this region is normally considered as a porous medium, whose permeability decreases and eventually vanishes with increasing amounts of solid fraction [1–16]. On the macroscopic level, two limiting cases can be identified in the description of the mushy zone behaviour [6]. In the first one, the solid is fully dispersed in the liquid phase, resulting in equal velocities for such phases. This model is applicable to amorphous materials (e.g. waxes and glasses) and to the equiaxed zone of a metal casting. In the second case, the solid matrix is distinct from the liquid and it is either fixed or moves with a prescribed velocity. In a physical sense, this model approximates the columnar dendritic zone of a solidifying metallurgical alloy. All these phenomena occur in a majority of solidification processes, where parts of the melt are at a temperature higher than the phase transition temperature.

Over the last years, several researchers have been devoted to the development of numerical, thermally coupled flow formulations, considering phase-change effects in order to simulate different engineering problems. In particular, a technological area of interest is the casting industry, where the temperature field, the phase-change front position and the heat transfer and flow patterns are crucial factors in obtaining sound parts. Numerical analyses related to the effects of natural convection on different phase-change processes have been discussed in several papers (see References [1–21] and references therein) in the framework of the well-known fixed domain enthalpy or source methods [1–17], front-tracking techniques [18–20] or adjoint formulations [21].

The aim of this work is to present a coupled solution for the incompressible Navier–Stokes equations (momentum, mass balance and energy equations), including phase-change effects in a primitive variable-based formulation, with a fixed domain discretization. The temperature-dependent density variation in the momentum equations is introduced via the Boussinesq model. The governing equations of the problem are presented in Section 2. In the context of the finite element method (FEM), the numerical solution of the incompressible Navier–Stokes equations is attempted via a staggered scheme, i.e. the coupled problem involves the numerical solution of the energy balance equation (thermal problem) together with the momentum and incompressibility equations (flow problem) and a coupling algorithm between these two problems, which guarantees a fully coupled numerical solution. The flow equations are solved using a generalized streamline operator (GSO) technique applied to incompressible flows [22–24]. The GSO approach circumvents the Babuska–Brezzi (BB) condition, providing stability in the solution of the pressure [25,26]. This technique also enables the use of equal-order interpolation functions for the primitive variables of the flow problem: velocity and pressure; both are defined for every node of the finite element mesh. Thus, the terms involving such variables are numerically integrated, employing the same standard Gaussian integration rule; avoiding, therefore, the reduced integration procedure for the pressure terms. Moreover, the standard penalization methods necessary to fulfil the incompressibility condition are not required in this case. These aspects have been illustrated in the solution of classical benchmark flow problems under isothermal conditions in References [22,23]. On the other hand, the energy equation is approached with a temperature-based generalized phase-change formulation using a simplified GSO methodology, where special attention is devoted to the

classical and advective phase-change terms [27–29]. In sharp contrast with other phase-change methods, it should be noted that these terms do not need any explicit regularization because an improved numerical integration procedure is used to compute them.

In this last context, the derived fully coupled finite element equations, which lead to an algorithm that provides stability and convergence of the numerical solution, constitutes the main original contribution of this work. Further, an incremental iterative Newton-type solution strategy is used to solve the non-linear system of equations corresponding to the flow and thermal problems, where the convergence criteria are written in terms of the respective residual vectors. A description of the proposed finite element formulation is presented in Section 3.

Finally, in Section 4, this formulation is used in the analyses of solidification and melting problems in order to validate the proposed methodology. To this end, the results obtained using the present formulation are compared with experimental observations and numerical results reported in the literature. The ability to deal with isothermal and non-isothermal phase-change cases, strongly coupled problems (high Rayleigh numbers) and temperature-dependent material properties are additional relevant features of this formulation, which will be discussed in these examples.

2. GOVERNING EQUATIONS

Let an open-bounded domain Ω be a spatial configuration of a continuum medium with spatial co-ordinates labelled by $\boldsymbol{x}$ (measured with respect to a reference co-ordinate system), let Γ be its smooth boundary and Υ be the time interval of interest ($t \in \Upsilon$).

The incompressible behaviour of fluids with phase-change effects can be described by the following equations:

equation of motion

$$\rho \dot{\boldsymbol{v}} + \rho(\boldsymbol{v} \cdot \nabla)\boldsymbol{v} + \nabla p - \nabla \cdot (2\mu \boldsymbol{\epsilon}) = \rho \boldsymbol{b} \quad \text{in } \Omega \times \Upsilon \tag{1}$$

continuity equation

$$\nabla \cdot \boldsymbol{v} = 0 \quad \text{in } \Omega \times \Upsilon \tag{2}$$

energy equation

$$\rho\left(c + L\frac{\partial f_{\mathrm{pc}}}{\partial T}\right)(\dot{T} + \nabla T \cdot \boldsymbol{v}) = \nabla \cdot (k \nabla T) + \rho r \quad \text{in } \Omega \times \Upsilon \tag{3}$$

together with adequate boundary and initial conditions [22,27] and an appropriate constitutive relation for the phase-change function f_{pc} [27–29]. In these equations, ρ is the density, $\boldsymbol{v}$ is the velocity vector, p is the pressure, μ is the dynamic viscosity, $\boldsymbol{\epsilon}$ is the rate of deformation tensor, ∇ is the gradient operator and the superposed dot denotes time derivative. The body force is

assumed to be given by the Boussinesq approximation: $\boldsymbol{b} = \boldsymbol{g}[1 - \alpha(T - T_{\text{ref}})]$, where $\boldsymbol{g}$ is the gravity vector, α is the thermal volumetric dilatation coefficient, T is the temperature and the subindex 'ref' indicates a reference value. Moreover, c is the specific heat capacity, L is the specific latent heat, k is the conductivity coefficient and r is the specific heat source. It should be noted that μ, c and k may be temperature-dependent, the energy terms derived from mechanical effects have been neglected and, besides, the isotropic Fourier law has been adopted to describe the heat conduction.

In a phase-change problem, $f_{\text{pc}} \in [0, 1]$ is defined according to the nature of the phase-change where, from a macroscopical point of view, f_{pc} can be written in terms of T [1–21,27–30]. For the isothermal phase-change case, $f_{\text{pc}} = H(T - \bar{T}_{\text{m}})$, with H being the Heaviside function and $\bar{T}_{\text{m}}$ the melting temperature. On the other hand, for the non-isothermal case, different forms for f_{pc} have been established and applied in the solution of solidification problems, such as the linear and quadratic functions, the lever rule, the Scheil's equation, etc. [12,28]. In this context, with $f_{\text{pc}} = 0$ and $f_{\text{pc}} = 1$ in the solid and liquid phases respectively, the dynamic viscosity can be defined as [3,6,11,30]

$$\mu = \frac{\mu_{\text{l}}}{f_{\text{pc}}} \tag{4}$$

where μ_{l} is the dynamic viscosity in the liquid phase. It should be noted that $\mu = \mu_{\text{l}}$ in the liquid phase, while for the solid phase μ approaches infinite. This last condition is equivalent to a constraint of a zero velocity field in the solid phase and, therefore, the momentum and continuity equations need not be solved in this region. Note that only these two limiting situations, i.e. $f_{\text{pc}} = 1$ and $f_{\text{pc}} = 0$, take place for the isothermal phase-change case, precluding in this way any regularization on the viscosity. Moreover, Equation (4) gives the viscosity law assumed to be valid in the mushy region for the non-isothermal phase-change case. This enhanced viscosity model corresponds better to the physical situation of equiaxed solidification, where free-floating crystals are transported with the melt at a unique velocity [3,6,11]. This approach differs from the enthalpy–porosity technique proposed in References [2,4,6,7], which consists, basically, in making the flow in the mushy region mimic flow in a porous media (normally fixed) by adding a velocity-dependent source term in the momentum equations. This porous medium formulation properly describes, for example, the growth of a columnar array of crystals, where the solid consists of attached dendrites and the interdendritic fluid trickles between them.

This paper focuses on the modelling of both isothermal and non-isothermal phase-change problems where, for this latter case, an equiaxed morphology is assumed to develop in the mushy region. Therefore, the viscosity expression (4) is adopted in this work to describe the material flow behaviour.

3. FINITE ELEMENT FORMULATION

The spatial discretization of Equations (1)–(3) is performed in the framework of the FEM [31]. To this end, a GSO technique is used in the corresponding weak form, which leads to the following algebraic system of equations:

$$\boldsymbol{R}_V \equiv \boldsymbol{F}_V - \boldsymbol{M}_V\dot{\boldsymbol{V}} - \boldsymbol{K}_V\boldsymbol{V} = \boldsymbol{0} \tag{5.1}$$

$$\boldsymbol{R}_T \equiv \boldsymbol{F}_T - (\boldsymbol{C} + \boldsymbol{C}_{\mathrm{pc}})\dot{\boldsymbol{T}} - (\boldsymbol{K}_T + \boldsymbol{K}_{\mathrm{ad}} + \boldsymbol{K}_{\mathrm{ad\text{-}pc}})\boldsymbol{T} = \boldsymbol{0} \tag{5.2}$$

where $\boldsymbol{R}_V$ is the flow residual vector, $\boldsymbol{F}_V$ is the body force vector, $\boldsymbol{M}_V$ is the mass matrix, $\boldsymbol{K}_V$ is the flow convection–diffusion matrix, $\boldsymbol{V}$ is the nodal flow unknowns vector (velocity and pressure), $\boldsymbol{R}_T$ is the thermal residual vector, $\boldsymbol{F}_T$ is the external thermal flux vector, $\boldsymbol{C}$ is the capacity matrix, $\boldsymbol{C}_{\mathrm{pc}}$ is the phase-change matrix, $\boldsymbol{K}_T$ is the conductivity matrix, $\boldsymbol{K}_{\mathrm{ad}}$ is the thermal advective matrix, $\boldsymbol{K}_{\mathrm{ad\text{-}pc}}$ is the thermal phase-change advective matrix and $\boldsymbol{T}$ is the nodal temperature vector. The element expressions of the vectors and matrices appearing in Equations (5.1) and (5.2) can be found in Schemes 1 and 2 respectively.

For the flow equation (5.1), Scheme 1 shows the total element expressions decomposed into the well-known terms of the standard Galerkin method (SG) and those obtained from the GSO methodology [22]. It should be noted that the boundary conditions are only considered in the SG formulation and that the matrix $\boldsymbol{K}_V$ is defined considering different contributions: the convection effects, the diffusion term and the boundary conditions related to the prescribed deviatoric part of the stress tensor $\boldsymbol{H}$ on the boundary Γ_H [22]. Moreover, the GSO technique affects the mass matrix $\boldsymbol{M}_V$, the $\boldsymbol{K}_V$ matrix in its convection and diffusion parts and the body force vector $\boldsymbol{F}_V$. As reported in Reference [22] for an isothermal flow formulation, these contributions are responsible for the stability and accuracy of the GSO methodology studied for the incompressible Navier–Stokes equations, where, in particular, a very good numerical behaviour can be observed in low-, moderated- and high-Reynolds number problems. The additional notation used in Scheme 1 is: $\boldsymbol{n}$ is the unit outward normal vector to the boundary, $\boldsymbol{N}_V$ is the flow shape function matrix such that $\boldsymbol{N}_V = \boldsymbol{N}^u + \boldsymbol{N}^p$, where $\boldsymbol{N}^u$ and $\boldsymbol{N}^p$ are the shape function matrices associated with the velocity and pressure degrees of freedom respectively; $\boldsymbol{A}_n$ is the generalized convection tensor defined for each fixed direction n ($n = 1, \ldots, n_{\mathrm{dim}}$; n_{dim} being the spatial dimension), where $\boldsymbol{A}_n = \boldsymbol{A}_n^u + \boldsymbol{A}_n^p$, with $\boldsymbol{A}_n^u$ and $\boldsymbol{A}_n^p$ being the components of $\boldsymbol{A}_n$ associated with, once more, the velocity and pressure degrees of freedom; $\boldsymbol{K}_{jn}$ is the generalized diffusion tensor written for each pair of fixed directions jn ($j = 1, \ldots, n_{\mathrm{dim}}$ and $n = 1, \ldots, n_{\mathrm{dim}}$); $\boldsymbol{M}$ is the generalized mass matrix; $\boldsymbol{F} = [\rho\boldsymbol{b}, 0]$ is the generalized body force vector; $\bar{p}$ is the prescribed pressure on Γ_p; and $\boldsymbol{\tau}_V$ is the 'flow upwinding tensor' computed according Reference [22] subject to certain design conditions detailed in Reference [24]. Note that $\boldsymbol{\tau}_V$ is defined in terms of $\boldsymbol{\tau}_{V_Y}$, which is the flow upwinding tensor in the eigenvector system (denoted by $\boldsymbol{Y}$) of the matrix-valued $\tilde{p}$-norm of the generalized convective tensor with eigenvalues λ_{c_i}. Moreover, λ_{k_i} are the lumped values of the matrix-value $\tilde{p}$-norm of the generalized diffusion tensor written in system $\boldsymbol{Y}$ and α_{V_i} are the so-called optimal upwind functions applied to γ_{V_i} for each direction i. Note that $i = 1, \ldots, n_{\mathrm{dim}} + 1$ includes the degrees of freedom for the velocity components and also that for the pressure. In addition, in the present work the choice for $\tilde{p}$ is 1.

The notation used in Scheme 2 to describe the thermal equation (5.2) is: $\boldsymbol{N}_T$ is the thermal shape function matrix; $\bar{q}$ is the prescribed normal heat flux on Γ_q; T_{env} is the temperature of the environment surrounding Ω; h is the heat transfer coefficient related to the convection–conduction–radiation phenomena between Ω and the environment through Γ_q, $\boldsymbol{F}_{\mathrm{c}}$ is the concentrated heat flux vector; and τ_T is the thermal upwinding parameter accounting for

phase-change effects in charge of avoiding local numerical oscillations in the vicinity of sharp gradients of f_{pc} [29]. In the computation of τ_T, α_T is the optimal upwind function applied to γ_T and l_{ch} is a characteristic element length. Further, it should be noted that particular expressions for $\boldsymbol{C}_{\mathrm{pc}}$ and $\boldsymbol{K}_{\text{ad-pc}}$, expressed in brackets in Scheme 2, can be derived for the isothermal phase-change case, where Γ_{pc} is the moving interface with temperature $\bar{T}_{\mathrm{m}}$, which separates the liquid and solid phases [27–29].

Element expressions of the discretized flow equation

♣ Mass matrix

$$\boldsymbol{M}_V = \boldsymbol{M}_{SG} + \boldsymbol{M}_{GSO}$$

♣ Convection-diffusion matrix

$$\boldsymbol{K}_V = \boldsymbol{K}^c + \boldsymbol{K}^\mu + \boldsymbol{K}^H$$

where

- $\boldsymbol{K}^c = \boldsymbol{K}^c_{SG} + \boldsymbol{K}^c_{GSO}$
- $\boldsymbol{K}^\mu = \boldsymbol{K}^\mu_{SG} + \boldsymbol{K}^\mu_{GSO}$
- $\boldsymbol{K}^H = \boldsymbol{K}^H_{SG}$

♣ Body force vector

$$\boldsymbol{F}_V = \boldsymbol{F}_{SG} + \boldsymbol{F}_{GSO} + \boldsymbol{H}_{SG}$$

Element expressions of the discretized flow equation corresponding to the standard Galerkin method

• Mass matrix

$$\boldsymbol{M}_{SG} = \int_{\Omega^{(e)}} \boldsymbol{N}_V^T \boldsymbol{M} \boldsymbol{N}_V d\Omega$$

• Generalized convection matrix

$$\boldsymbol{K}^c_{SG} = \int_{\Omega^{(e)}} \boldsymbol{N}_V^T \boldsymbol{A}^u_n \nabla_n \boldsymbol{N}^u d\Omega - \int_{\Omega^{(e)}} (\nabla_n \boldsymbol{N}_V)^T \boldsymbol{A}^p_n \boldsymbol{N}^p d\Omega$$

• Generalized diffusion matrix

$$\boldsymbol{K}^\mu_{SG} = \int_{\Omega^{(e)}} (\nabla_j \boldsymbol{N}_V)^T \boldsymbol{K}_{jn} \nabla_n \boldsymbol{N}_V d\Omega + \int_{\Gamma^{(e)}_p} \boldsymbol{N}^{uT} n_j \boldsymbol{K}_{jn} \nabla_n \boldsymbol{N}_V d\Gamma$$

• Pressure term matrix

$$\boldsymbol{K}^H_{SG} = \int_{\Gamma^{(e)}_H} \boldsymbol{N}^{uT} \boldsymbol{n}^T \boldsymbol{N}^p d\Gamma$$

• Generalized body force vector

$$\boldsymbol{F}_{SG} = \int_{\Omega^{(e)}} \boldsymbol{N}_V^T \boldsymbol{F} d\Omega$$

• Generalized vector of imposed surface forces

$$\boldsymbol{H}_{SG} = \int_{\Gamma^{(e)}_H} \boldsymbol{N}_V^T \boldsymbol{H} d\Gamma + \int_{\Gamma^{(e)}_p} \boldsymbol{N}^{uT} \boldsymbol{n}^T \bar{p} d\Gamma$$

Element expressions of the discretized flow equation corresponding to the generalized streamline operator method

• Mass matrix

$$\boldsymbol{M}_{GSO} = \int_{\Omega^{(e)}} \boldsymbol{P}_V^T \boldsymbol{M} \boldsymbol{N}_V d\Omega$$

• Generalized convection matrix

$$\boldsymbol{K}^c_{GSO} = \int_{\Omega^{(e)}} \boldsymbol{P}_V^T \boldsymbol{A}_n \nabla_n \boldsymbol{N}_V d\Omega$$

• Generalized diffusion matrix

$$\boldsymbol{K}^\mu_{GSO} = -\int_{\Omega^{(e)}} \boldsymbol{P}_V^T \nabla_j \boldsymbol{K}_{jn} \nabla_n \boldsymbol{N}_V d\Omega$$

• Generalized body force vector

$$\boldsymbol{F}_{GSO} = \int_{\Omega^{(e)}} \boldsymbol{P}_V^T \boldsymbol{F} d\Omega$$

• Perturbation function

$$\boldsymbol{P}_V = \boldsymbol{\tau}_V \, \boldsymbol{A}_n \, \nabla_n \boldsymbol{N}_V$$

Flow upwinding tensor

$$\boldsymbol{\tau}_V = \boldsymbol{Y} \cdot \boldsymbol{\tau}_{V_Y} \cdot \boldsymbol{Y}^{-1}$$

where

$\boldsymbol{\tau}_{V_Y}$: *diagonal tensor with components* τ_i $(i = 1, \ldots, n_{dim} + 1)$

$$\tau_i = \begin{cases} 0 & \text{if } \lambda_{c_i} = 0 \\ \dfrac{\alpha_{V_i}}{\lambda_{c_i}} & \text{if } \lambda_{c_i} \neq 0 \text{ and } \lambda_{k_i} \neq 0 \\ \dfrac{1}{\lambda_{c_i}} & \text{if } \lambda_{c_i} \neq 0 \text{ and } \lambda_{k_i} = 0 \end{cases}$$

with

$$\alpha_{V_i} = coth(\gamma_{V_i}) - 1/\gamma_{V_i}$$

$$\gamma_{V_i} = \frac{\lambda_{c_i}}{\lambda_{k_i}}$$

Scheme 1. Element expressions of the discretized flow equation.

Element expressions of the discretized thermal equation

♣ External thermal flux vector

$$\boldsymbol{F}_T = \int_{\Omega^{(e)}} \boldsymbol{W}_T^{\mathcal{T}}\, \rho\, r\, d\Omega + \int_{\Gamma_q^{(e)}} \boldsymbol{N}_T^{\mathcal{T}}\, \bar{q}\, d\Gamma_q + \int_{\Gamma_q^{(e)}} \boldsymbol{N}_T^{\mathcal{T}}\, h\, T_{env}\, d\Gamma_q + \sum_{i=1}^{n_c} \boldsymbol{F}_{c_i}^{(e)}$$

♣ Capacity matrix

$$\boldsymbol{C} = \int_{\Omega^{(e)}} \boldsymbol{W}_T^{\mathcal{T}}\, \rho\, c\, \boldsymbol{N}_T\, d\Omega$$

♣ Phase-change matrix

$$\boldsymbol{C}_{pc} = \int_{\Omega^{(e)}} \boldsymbol{W}_T^{\mathcal{T}}\, \rho\, L\, \frac{\partial f_{pc}}{\partial T}\, \boldsymbol{N}_T\, d\Omega \qquad \left(\boldsymbol{C}_{pc} = \int_{\Gamma_{pc}} \boldsymbol{W}_T^{\mathcal{T}}\, \frac{\rho\, L}{|\nabla T|_{\bar{T}_m}}\, \boldsymbol{N}_T\, d\Gamma_{pc}\right)$$

♣ Conductivity matrix

$$\boldsymbol{K}_T = \int_{\Omega^{(e)}} (\nabla \boldsymbol{N}_T)^{\mathcal{T}}\, k\, \nabla \boldsymbol{N}_T\, d\Omega + \int_{\Gamma_q^{(e)}} \boldsymbol{N}_T^{\mathcal{T}}\, h\, \boldsymbol{N}_T\, d\Gamma_q + \int_{\Omega^{(e)}} (\boldsymbol{W}_T - \boldsymbol{N}_T)^{\mathcal{T}}\, \nabla(k\, \nabla \boldsymbol{N}_T)\, d\Omega$$

♣ Thermal advective matrix

$$\boldsymbol{K}_{ad} = \int_{\Omega^{(e)}} \boldsymbol{W}_T^{\mathcal{T}}\, \rho\, c\, \boldsymbol{v}\, \nabla \boldsymbol{N}_T\, d\Omega$$

♣ Thermal phase-change advective matrix

$$\boldsymbol{K}_{ad-pc} = \int_{\Omega^{(e)}} \boldsymbol{W}_T^{\mathcal{T}}\, \rho\, L\, \frac{\partial f_{pc}}{\partial T}\, \boldsymbol{v}\, \nabla \boldsymbol{N}_T\, d\Omega \qquad \left(\boldsymbol{K}_{ad-pc} = \int_{\Gamma_{pc}} \boldsymbol{W}_T^{\mathcal{T}}\, \frac{\rho\, L}{|\nabla T|_{\bar{T}_m}}\, \boldsymbol{v}\, \nabla \boldsymbol{N}_T\, d\Gamma_{pc}\right)$$

• Weight function matrix

$$\boldsymbol{W}_T = \boldsymbol{N}_T + \boldsymbol{P}_T$$

• Perturbation function

$$\boldsymbol{P}_T = \tau_T\, \boldsymbol{v}\, \nabla \boldsymbol{N}_T$$

Thermal upwinding parameter

$$\tau_T = \frac{\alpha_T\, l_{ch}}{2\ |\boldsymbol{v}|}$$

with

$$\alpha_T = coth(\gamma_T) - 1/\gamma_T$$

$$\gamma_T = \frac{\rho\ (c + L\frac{\partial f_{pc}}{\partial T})\ |\boldsymbol{v}|\ l_{ch}}{2\ k}$$

Scheme 2. Element expressions of the discretized thermal equation.

As f_{pc} can present a discontinuity inside an element for the isothermal phase-change case, a non-standard numerical integration, consisting of splitting the integral over the element domain into liquid and solid element sub-domains integrals, such that a continuous phase-change function is defined in such regions (see, e.g. Reference [27]), is used in the present work to accurately integrate the phase-change and viscosity terms. With these considerations, an explicit regularization of f_{pc}, and consequently on μ, is not needed.

The temporal discretization of system (5) is performed using an implicit backward Euler scheme [31]. Further, this coupled system of equations is solved with a staggered incremental iterative strategy, where the convergence criteria are written in terms of the residual vectors, where ε_V and ε_T are the admissible tolerances of the out-of-balance residuals for the flow and thermal problems respectively, taken in the range of 10^{-6}–10^{-3} throughtout this work.

For a given step, the global convergence is obtained when the local convergence conditions, corresponding to locally converged flow and thermal solutions computed in a consecutive manner using an iterative Newton–Raphson-type algorithm in the solution of each problem, are simultaneously achieved. This staggered scheme is detailed in Scheme 3. Note that this strategy differs from the more relaxed numerical procedure extensively used in the solution of

heat and fluid flow problems (see, e.g. Reference [30]) in which the coupled solution is shifted in time as no global iterations are performed within the same time step when solving the two problems in a consecutive form, i.e. the global convergence is not strictly fulfilled at the end of a given time step.

Staggered scheme for the thermally coupled flow formulation:
the Iterative-Converged-Consecutive strategy

Thermally coupled flow problem at time $t + \Delta t$ *(a known solution is assumed at time* t*)*

I. *Initial conditions* $\boldsymbol{T}^{0,0} = {}^t\boldsymbol{T}$ *and* $\boldsymbol{V}^{0,0} = {}^t\boldsymbol{V}$

II. *Global iterative solution (global iteration index* $k = 1, ..., n_G$*)*

II.1 *flow problem*

♣ *input* $\boldsymbol{I}_{TV}^{i,k} = [\boldsymbol{T}^{i,k}, \boldsymbol{f}_{pc}^{i,k}]$

♣ *local iterative solution (local iteration index* $j = 1, ..., n_V$*)*

$$\boldsymbol{J}_{VV}^{j-1,k} \Delta \boldsymbol{V}^{j,k} = \boldsymbol{R}_V^{j-1,k}$$

$$\boldsymbol{V}^{j,k} = \boldsymbol{V}^{j-1,k} + \Delta \boldsymbol{V}^{j,k}$$

$$\frac{\|\boldsymbol{R}_V^{j,k}\|_{L_2}}{\|\boldsymbol{F}_V^{j,k}\|_{L_2}} < \varepsilon_V$$

♣ *output* $\boldsymbol{I}_{VT}^{j,k} = [\boldsymbol{V}^{j,k}]$ *and* $\boldsymbol{V}^{0,k+1} = \boldsymbol{V}^{j,k}$

II.2 *thermal problem*

♣ *input* $\boldsymbol{I}_{VT}^{j,k} = [\boldsymbol{V}^{j,k}]$

♣ *local iterative solution (local iteration index* $i = 1, ..., n_T$*)*

$$\boldsymbol{J}_{TT}^{i-1,k} \Delta \boldsymbol{T}^{i,k} = \boldsymbol{R}_T^{i-1,k}$$

$$\boldsymbol{T}^{i,k} = \boldsymbol{T}^{i-1,k} + \Delta \boldsymbol{T}^{i,k}$$

$$\frac{\|\boldsymbol{R}_T^{i,k}\|_{L_2}}{\|\boldsymbol{F}_T^{i,k}\|_{L_2}} < \varepsilon_T$$

♣ *output* $\boldsymbol{I}_{TV}^{i,k} = [\boldsymbol{T}^{i,k}, \boldsymbol{f}_{pc}^{i,k}]$ *and* $\boldsymbol{T}^{0,k+1} = \boldsymbol{T}^{i,k}$

II.3 *global convergence*

$$\frac{\|\boldsymbol{R}_V^{j,k}\|_{L_2}}{\|\boldsymbol{F}_V^{j,k}\|_{L_2}} < \varepsilon_V \quad \text{and} \quad \frac{\|\boldsymbol{R}_T^{i,k}\|_{L_2}}{\|\boldsymbol{F}_T^{i,k}\|_{L_2}} < \varepsilon_T$$

Staggered scheme for the thermally coupled flow formulation: notation

- $\boldsymbol{J}_{VV}$ *and* $\boldsymbol{J}_{TT}$ *are the Jacobian matrices obtained in the standard manner as :*
$$\boldsymbol{J}_{VV} = -\frac{\partial \boldsymbol{R}_V}{\partial \boldsymbol{V}} \quad \text{and} \quad \boldsymbol{J}_{TT} = -\frac{\partial \boldsymbol{R}_T}{\partial \boldsymbol{T}}$$
- $\boldsymbol{V}$, $\boldsymbol{T}$ *and* $\boldsymbol{f}_{pc}$ *are the nodal vectors of the flow unknowns (velocity and pressure), temperature and phase − change function respectively.*
- n_G *is the maximum number of global iterations for the thermally coupled flow problem.*
- n_V *and* n_T *are the maximum number of local iterations for the flow and thermal problems respectively.*
- ε_V *and* ε_T *are the admissible tolerances of the out − of − balance residuals for the flow and thermal problems respectively.*
- $\| * \|_{L_2}$ *is the well − known norm in the* L_2 *space.*

Scheme 3. Staggered scheme for the thermally coupled flow formulation.

Table I. Aluminium properties.

Conductivity (k)	229.44 W (m °C)$^{-1}$
Specific heat (c)	1057.63 J (kg °C)$^{-1}$
Latent heat (L)	397765.0 J kg^{-1}
Density (ρ)	2650.0 kg m^{-3}
Dynamic viscosity of the liquid phase (μ_l)	3.233×10^{-3} kg (m s)$^{-1}$
Thermal dilatation coefficient (α)	3.84×10^{-5} °C^{-1}
Melting temperature ($\bar{T}_m$)	660.0°C

4. NUMERICAL EXAMPLES

4.1. Solidification of pure aluminium in a square region

A study of the natural convection during the solidification of a pure metal in a square enclosure is performed in this example. This problem has been analysed by several authors with different techniques in order to evaluate the influence of the flow pattern over the phase-change front position [18–20]. The material studied is aluminium with thermophysical properties presented in Table I, where, in this case, the phase-change takes place in an isothermal way. As described in Section 2, only two limiting situations, indicated by $f_{pc} = 1$ and $f_{pc} = 0$ respectively related to the liquid and solid phases existing in the material during the process, are considered in the analysis. Initially, the fluid in rest has a uniform temperature of $T_0 = 860$°C and this value is also considered as the reference temperature to be used in the Boussinesq approximation.

A convection–radiation heat transfer condition is applied in the left vertical wall with an environment temperature of 25°C and a Biot number ($Bi = L_{ch}h/k$, with L_{ch} being a characteristic length assumed to coincide with the cavity side and h the convection–radiation heat transfer coefficient) selected as 3.3. The other walls are insulated. Moreover, the velocity is fixed to zero in the whole boundary.

A set of different Rayleigh numbers has been analysed in the present study. The Rayleigh numbers ($R_a = g\alpha(T_0 - \bar{T}_m)L_{ch}^3\rho^2 c/(\mu k)$, with $g = 9.8$ m s^{-2}) studied are: 0, 10^4, 10^5, 10^6 and 10^7, obtained in this problem by varying the value of the cavity side. In addition, for this problem, the Prandtl number ($Pr = \mu c/k$) is 0.0149, while the Stefan number ($Ste = c(T_0 - \bar{T}_m)/L$) is 0.5317.

A non-uniform structured mesh (with a progressive linear refinement near the walls to properly describe the natural boundary conditions in the adiabatic walls) of 50×50 four-noded isoparametric elements has been employed in the domain discretization. The dimensionless time steps used in the transient analysis are (the characteristic scale for time is $L_{ch}^2\rho c/k$): $\Delta t = 0.01$ for $R_a = 0$, 10^4, 10^5 and 10^6; and 0.0025 ($\Delta t/4$) for $R_a = 10^7$. In this latter case, the reduction in Δt is justified for the sake of properly simulating the effects caused by the initial high temperature rates.

The velocity vector field and the isothermal curves at different dimensionless times of the analysis for $R_a = 10^5$ are respectively shown in Figures 1 and 2. Similar results for $R_a = 10^6$ and $R_a = 10^7$ are presented in Figures 3 and 4 and Figures 5 and 6. It is possible to note the flow pattern variation during the solidification process and, in particular, the secondary vortex

formation and its starting time, which decreases for larger Rayleigh numbers (in Figures 1, 3 and 5, the vector scale is not the same). As the Rayleigh number increases, the convective effects become more apparent and the isotherm lines progressively distort. Moreover, the curvature of the isotherms owing to the natural convection, leading to different phase-change front positions at the bottom and top parts of the cavity, which denote a faster solidification growth near the bottom of the enclosure, can also be seen.

In Table II, the dimensionless solidification times obtained in the present work at different Rayleigh numbers are compared in good agreement with those published in Reference [19] using a front-tracking method. Results achieved using the proposed formulation with a

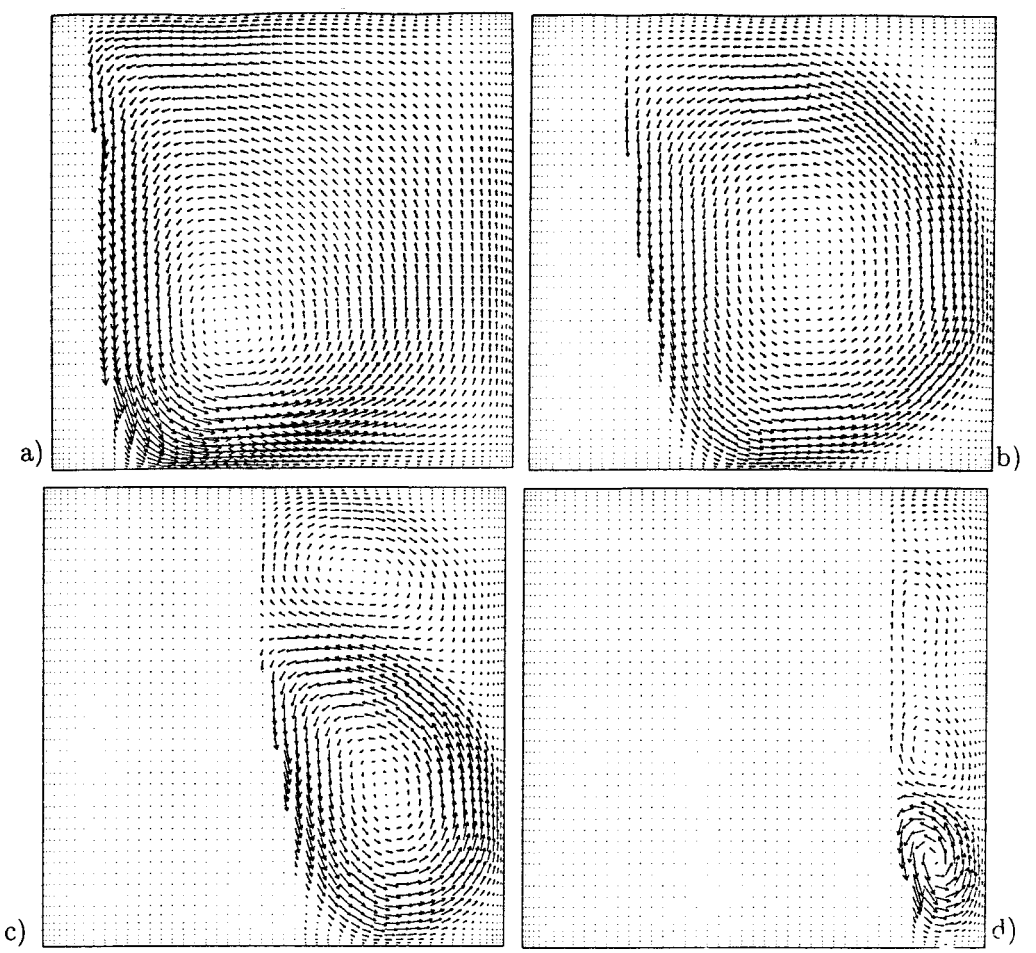

Figure 1. Solidification of pure aluminium in a square region. Velocity field for $R_a = 10^5$ at dimensionless times (a) 0.05, (b) 0.15, (c) 0.35 and (d) 0.60.

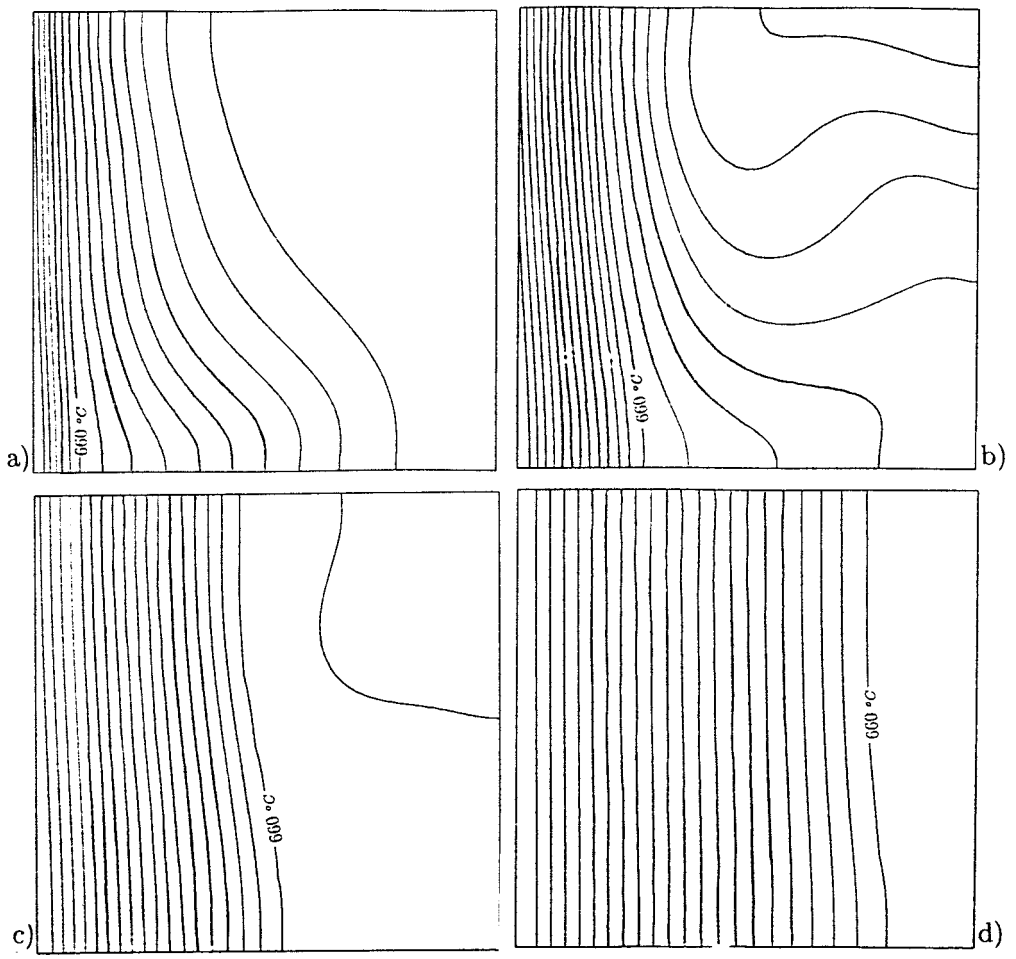

Figure 2. Solidification of pure aluminium in a square region. Temperature field for $R_a = 10^5$ at dimensionless times (a) 0.05, (b) 0.15, (c) 0.35 and (d) 0.60 (the isotherms are 20°C apart).

uniform 20×20 mesh are also enclosed in this table, showing a good performance for this coarse mesh. Choosing the solidification time of the advectionless case ($R_a = 0$ or the Stefan problem [1–21,27]) as a reference value, it can be observed that this parameter increases for $R_a = 10^4$ but decreases for $R_a = 10^5$, 10^6 and 10^7 when using the 50×50 mesh (a slightly different tendency is appreciated with the 20×20 mesh). Also note that this trend is completely similar to that reported in Reference [19].

The maximun dimensionless velocity values (the characteristic scale for velocity is $k/(\rho c L_{\mathrm{ch}})$) for $R_a = 10^5$, 10^6 and 10^7 at different dimensionless times of the analysis are presented in Table III; again in good comparison with the mentioned reference. Once more, results obtained with

the 20×20 mesh are included. For $R_a = 10^5$, the velocity field is shown to grow as the process proceeds in time reaching a peak before it eventually dies out. A similar trend is observed for $R_a = 10^6$ and 10^7 with peak values shifted to earlier stages of the solidification. The comparison of the results obtained with the two meshes shows some differences for large Rayleigh numbers mainly at the initial times of the analysis. The maximum characteristic Reynolds' numbers ($R_e = |\boldsymbol{v}_{\max}| L_{\text{ch}} \rho / \mu$) for these cases are: 1700, 5600 and 11000. Although this last value may denote a transitional flow for a given time of the analysis, laminar flow is assumed during the whole process. These results also show the ability of this formulation to deal with strongly thermally coupled flow problems (high R_a).

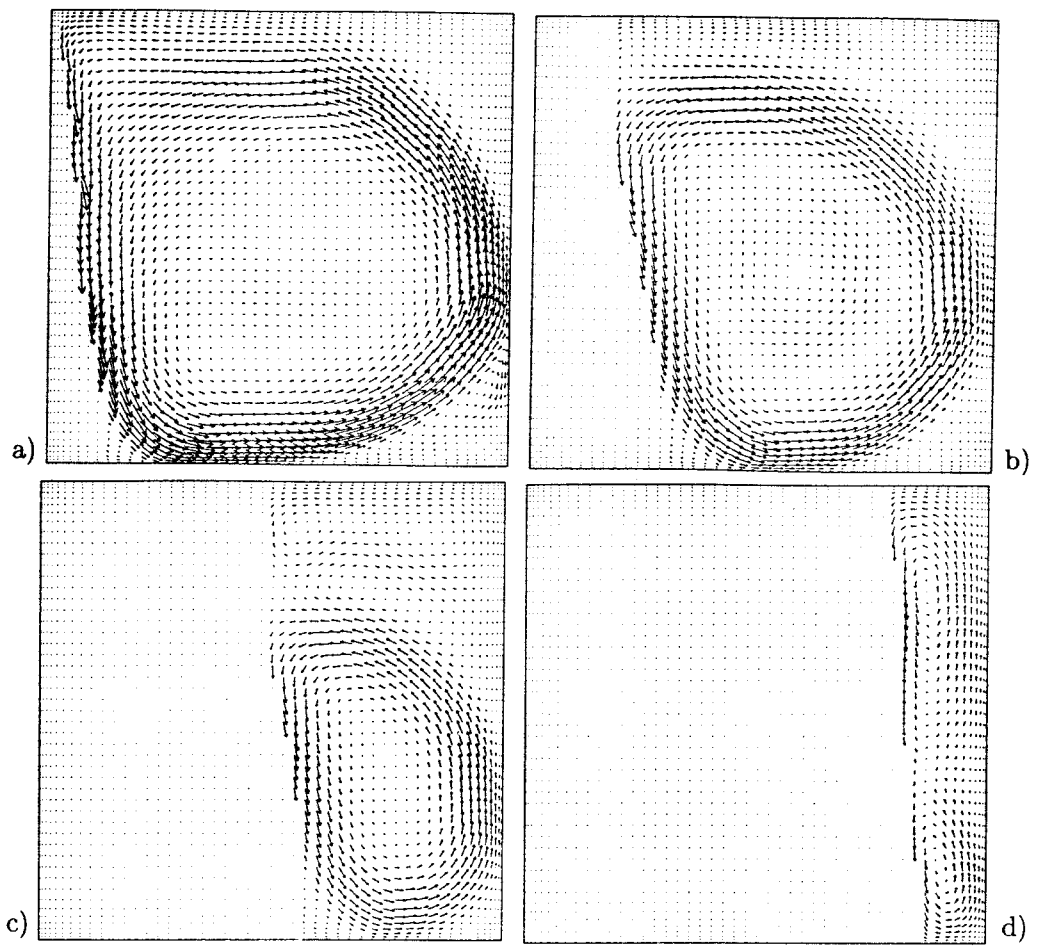

Figure 3. Solidification of pure aluminium in a square region. Velocity field for $R_a = 10^6$ at dimensionless times (a) 0.05, (b) 0.15, (c) 0.35 and (d) 0.60.

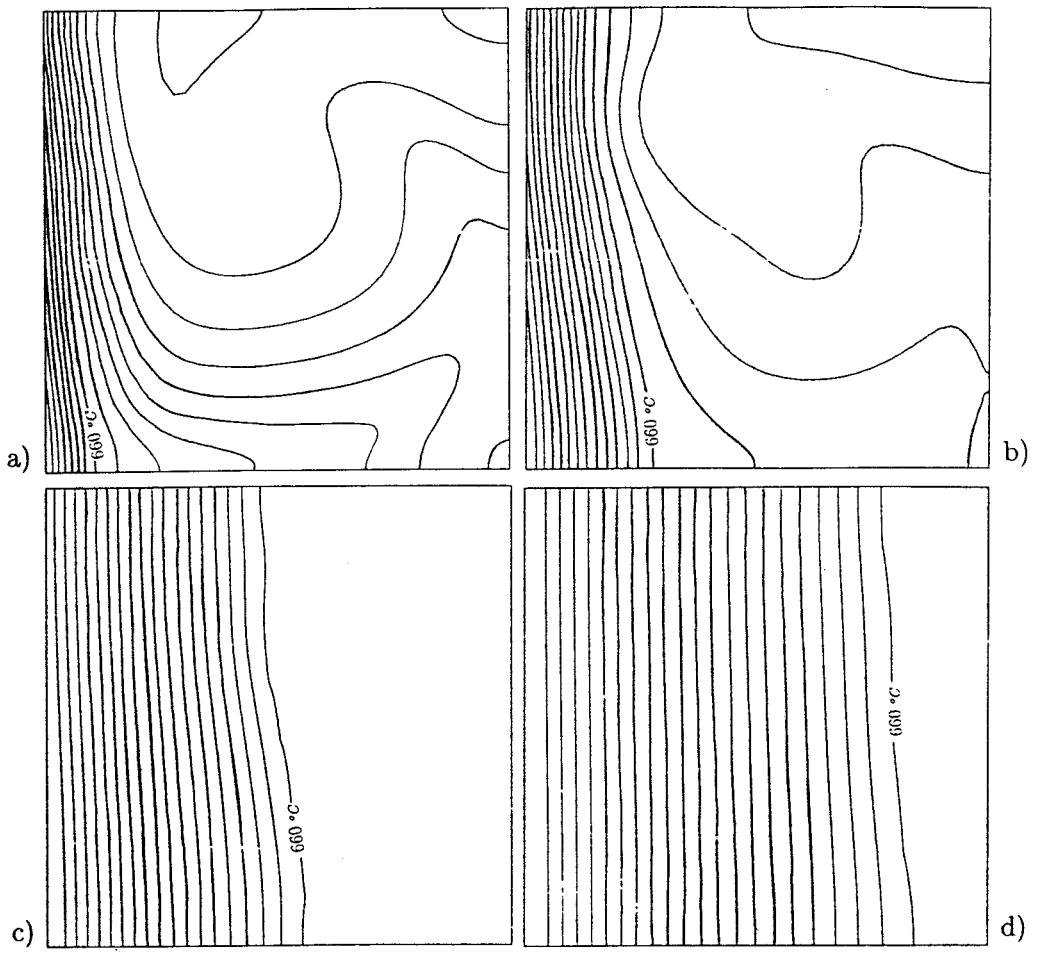

Figure 4. Solidification of pure aluminium in a square region. Temperature field for $R_a = 10^6$ at dimensionless times (a) 0.05, (b) 0.15, (c) 0.35 and (d) 0.60 (the isotherms are 20°C apart).

The phase-change front position at different dimensionless times and Rayleigh numbers, all of them obtained with the present formulation, are plotted in Figure 7. This figure clearly shows the important influence of R_a on the flow characterization and the heat transfer conditions. The front inclination with respect to the vertical position corresponding to $R_a = 0$ can be appreciated. Further, its high deviation at early times owing to the upper secondary vortex and the advanced position (in comparison with the $R_a = 0$ front position) in the final times of the process at high Rayleigh numbers is due to the natural convection and the developed velocity field. This last behaviour clarifies the reduction in the dimensionless solidification times shown in Table II.

Finally, in Figure 8, the obtained phase-change front position for $R_a = 10^5$ and 10^6 at different times of the process are drawn in comparison with the curves computed in Reference [19] where, once more, it should be noted that the results given by the fixed domain technique used in the present work and those corresponding to the front tracking method of Reference [19] are in a good agreement.

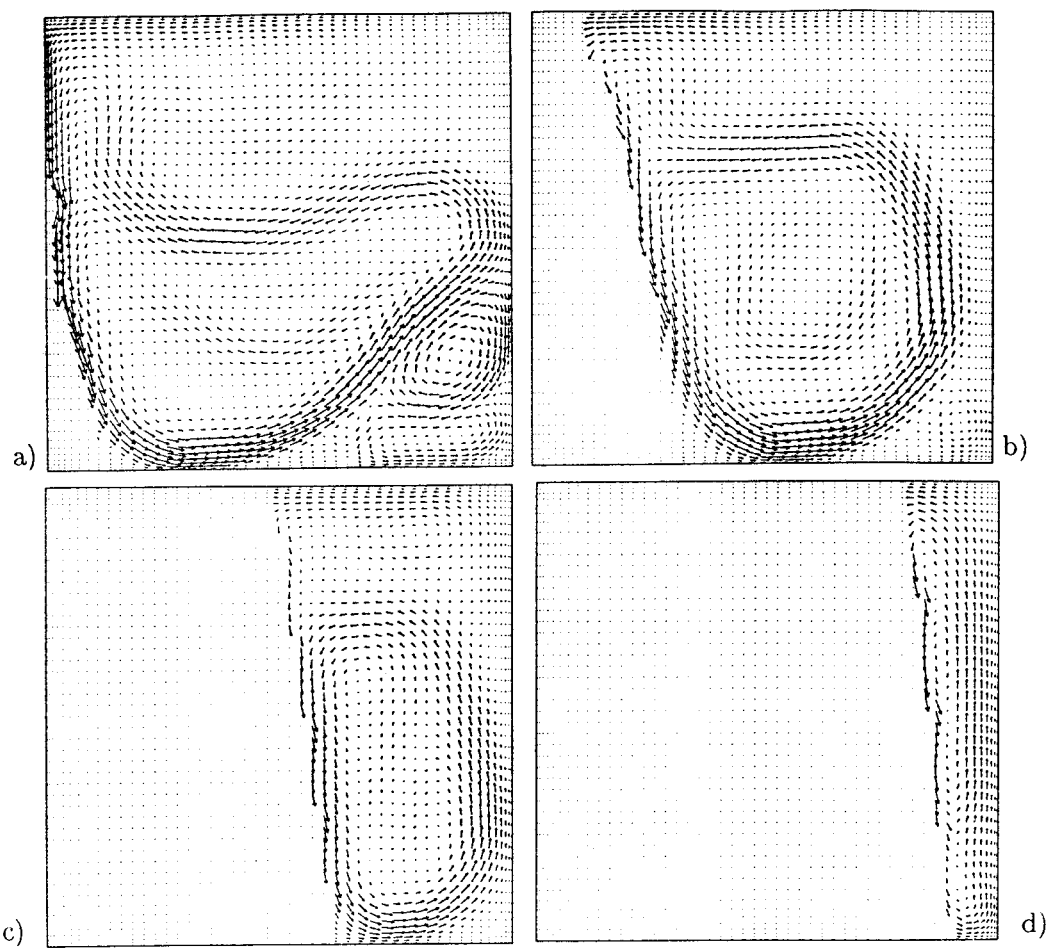

Figure 5. Solidification of pure aluminium in a square region. Velocity field for $R_a = 10^7$ at dimensionless times (a) 0.05, (b) 0.15, (c) 0.35 and (d) 0.60.

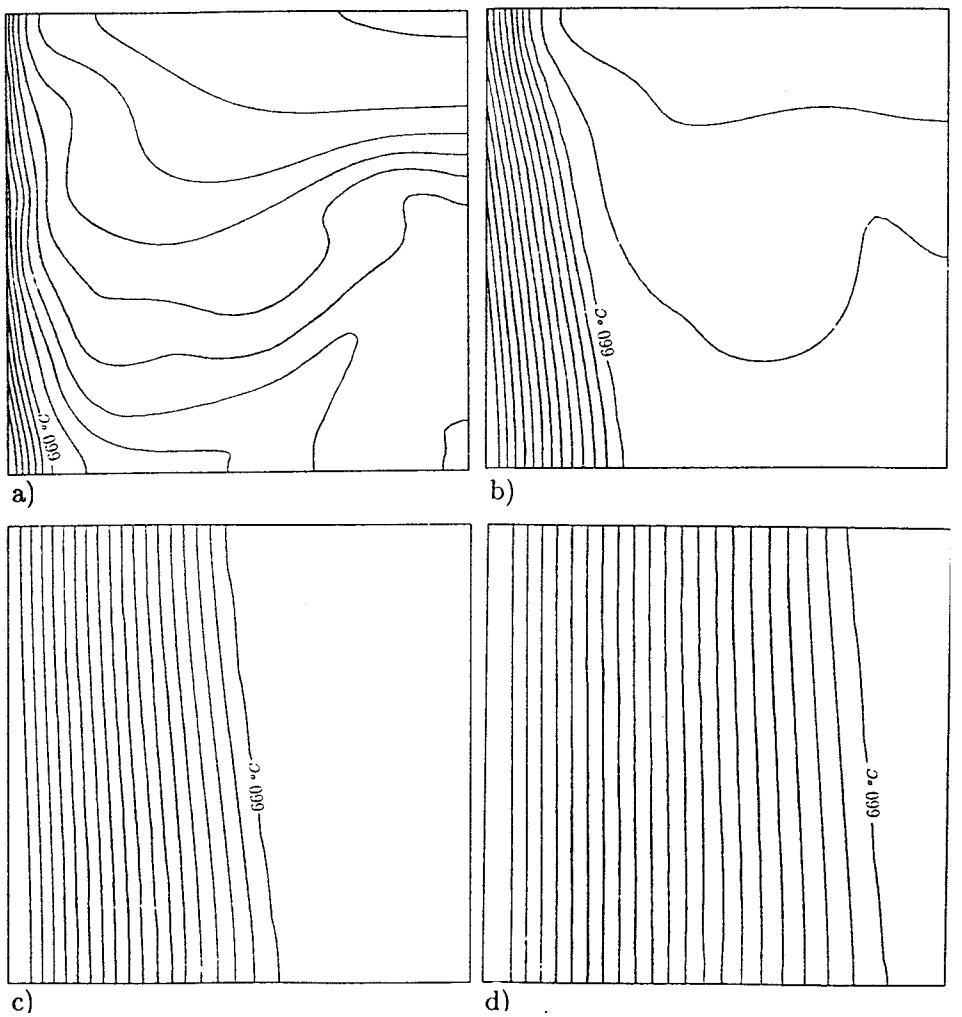

Figure 6. Solidification of pure aluminium in a square region. Temperature field for $R_a = 10^7$ at dimensionless times (a) 0.05, (b) 0.15, (c) 0.35 and (d) 0.60 (the isotherms are 20°C apart).

4.2. Melting of gallium in a rectangular region

Several experiments for melting of pure metal gallium with buoyancy-induced flow in order to measure the effect of convection on the solid–liquid interface motion have been reported in Reference [32]. This problem has been simulated by many researchers (see References [4,11,19] and references therein) using different fixed grid or front-tracking techniques. The aim of the present analysis is, therefore, to validate the proposed fixed-domain temperature-based formulation with experimental and numerical results derived from existing modelling techniques. The

Table II. Solidification of pure aluminium in a square region. Dimensionless solidification times at different Rayleigh numbers.

Rayleigh number	Present work (20×20)	Present work (50×50)	McDaniel and Zabaras [19]
0.0	0.834	0.840	0.840
10^4	0.841	0.848	0.847
10^5	0.836	0.834	0.833
10^6	0.830	0.822	0.813
10^7	0.792	0.811	

material properties for pure gallium can be found in Table IV [19]. The narrow temperature range (less than 10°C) used in the experiments carried out in Reference [32] allows the assumption of constant physical properties. Moreover, although the thermal conductivity of gallium is anisotropic, the choice of an isotropic conductivity for the simulation is clearly justified by the arguments given in Reference [4]. The melting experiment is modelled in a vertical, two-dimensional rectangular enclosure of aspect ratio = 2 (height = 0.045 m and width = 0.09 m). The initial temperature is 28.3°C. A value of 36.0°C is prescribed in the left wall, while the other sides are assumed insulated. The velocity is constrained in all the walls. The melting temperature corresponds to 29.8°C, which is also chosen as a reference value [19,32]. Once again, the already mentioned considerations related to f_{pc} under isothermal phase-change conditions are also taken into account in this analysis. For this problem, the Rayleigh (with $g = 9.8\ \mathrm{m\ s^{-2}}$), Prandtl and Stefan numbers correspond to 2.2×10^5, 0.021 and 0.042, respectively.

Table III. Solidification of pure aluminium in a square region. Maximum dimensionless velocity values at different dimensionless times and Rayleigh numbers.

Rayleigh number/time	Present work (20×20)	Present work (50×50)	McDaniel and Zabaras [19]
$R_a = 10^5$			
$t = 0.05$	25.0	24.9	24.1
$t = 0.15$	25.5	27.1	26.1
$t = 0.35$	16.2	16.8	15.5
$t = 0.60$	1.8	2.3	1.9
$R_a = 10^6$			
$t = 0.05$	83.7	96.4	105.1
$t = 0.15$	47.3	58.1	51.4
$t = 0.35$	23.2	25.2	22.0
$t = 0.60$	2.2	2.8	2.0
$R_a = 10^7$			
$t = 0.05$	165.3	371.0	
$t = 0.15$	75.6	108.6	
$t = 0.35$	25.4	24.3	
$t = 0.60$	6.0	10.5	

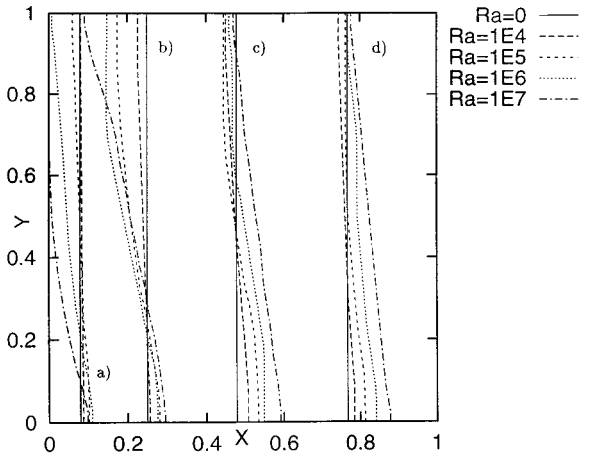

Figure 7. Solidification of pure aluminium in a square region. Phase-change front position for $R_a = 0$, 10^4, 10^5, 10^6 and 10^7 at dimensionless times (a) 0.05, (b) 0.15, (c) 0.35 and (d) 0.60.

The uniform finite element mesh considered in the analysis is composed of 20×40 isoparametric four-noded elements. The time step used was 7.355 s. Figures 9 and 10 show respectively the velocity field and the phase-change front location at different times of the process. At the beginning of the analysis, the melt front is almost planar, as the natural convection field has just begun to develop. Once the natural convection has intensified, it starts to have a pronounced influence on the overall energy transport from the heated wall to the melt. From Figure 9 it can be seen that a main vortex appears at the upper part of the liquid region, where the maximum values of the velocity norm are approximated to those reported in

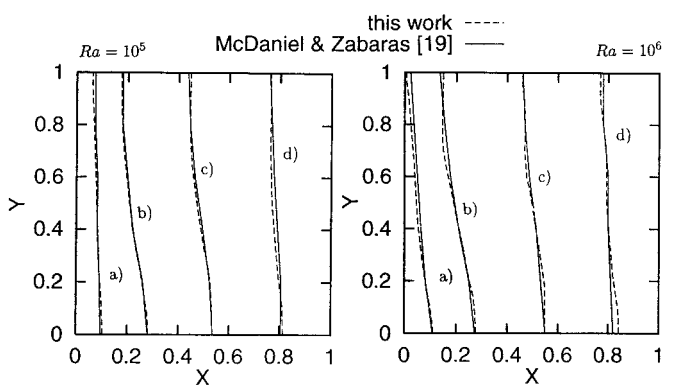

Figure 8. Solidification of pure aluminium in a square region. Phase-change front position for $R_a = 10^5$ and 10^6 at dimensionless times (a) 0.05, (b) 0.15, (c) 0.35 and (d) 0.60.

Table IV. Gallium properties.

Conductivity (k)	32.0 W (m °C)$^{-1}$
Specific heat (c)	381.5 J (kg °C)$^{-1}$
Latent heat (L)	80160.0 J kg^{-1}
Density (ρ)	6095.0 kg m^{-3}
Dynamic viscosity of the liquid phase (μ_l)	1.81×10^{-3} kg (m s)$^{-1}$
Thermal dilatation coefficient (α)	1.20×10^{-4} °C^{-1}
Melting temperature ($\bar{T}_m$)	29.78°C

Reference [19]. The influence of convection currents intensifies with time such that the morphology of the melt front becomes more acute as melting progresses. Although the upper section of the melt front advances rapidly owing to fluid motion, the lower section moves considerably slower, thereby resulting in the acute shape illustrated in Figure 10. Moreover, the computed front position history compares reasonably well with the experimental data and the numerical results of Reference [19]. The small discrepancies between the measured and computed results may be attributed to different factors, such as three-dimensional effects in the experimental apparatus used to determine the front position and variations in fluid properties. As reported in Reference [11], other sources of discrepancy may be attributed to the multiple-cell formation occurring at the early stages of the process when the fluid cavity thickness is approximately 0.96 mm. Although this last effect is out of the spatial scale considered in the present analysis, the numerical predictions of the front position, as mentioned above, show a reasonable overall agreement with the available published results for the aspect ratio studied in this paper.

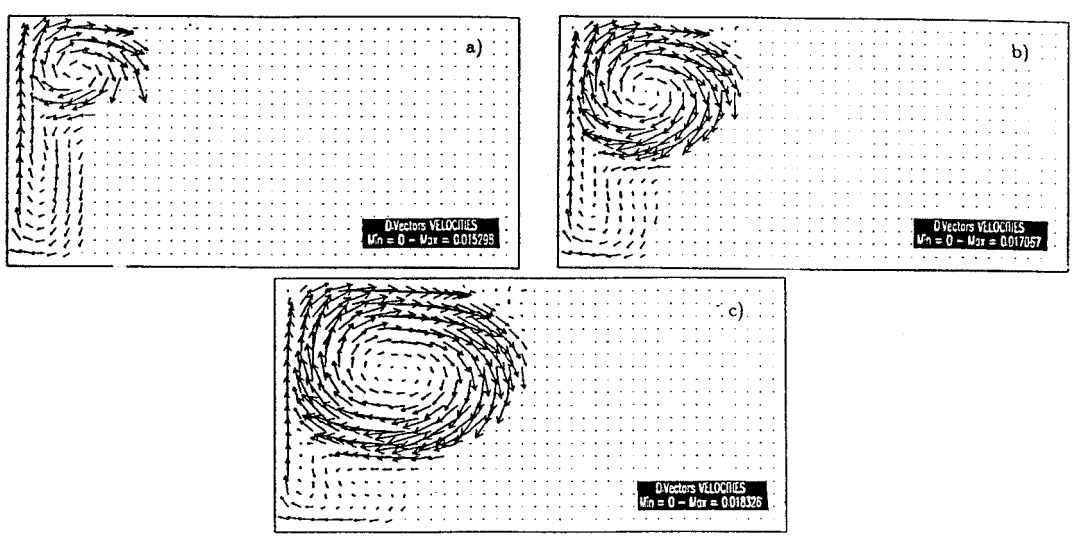

Figure 9. Melting of gallium in a rectangular region. Velocity field at times (a) 300 s, (b) 480 s and (c) 720 s.

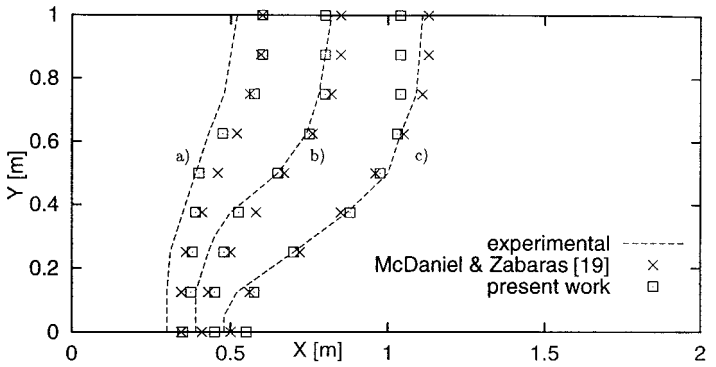

Figure 10. Melting of gallium in a rectangular region. Phase-change front location at times (a) 300 s, (b) 480 s and (c) 720 s.

4.3. A mushy region test problem

A natural convection test consisting of a confined flow in a square cavity (1×1) is presented. This test has been analysed in Reference [2] to evaluate the mushy zone behaviour during the material solidification. All the problem data is given in dimensionless values. The initial cavity temperature is 0.5 and this value, also adopted as a reference temperature, is kept during the whole process on the right vertical wall. The cooling begins when the temperature at the left vertical wall is prescribed to -0.5. The other walls are adiabatic and, as usual in this kind of problem, the velocity is constrained in the cavity boundary. The gravity constant is $g = 1000$. Further, the phase-change function f_{pc} is defined according to a linear form as [2]

$$f_{\mathrm{pc}} = \begin{cases} 0 & , \ \forall T \le \bar{T}_{\mathrm{s}} \\ 0 < \dfrac{T - \bar{T}_{\mathrm{s}}}{\bar{T}_{\mathrm{l}} - \bar{T}_{\mathrm{s}}} \le 1 & , \ \bar{T}_{\mathrm{s}} < \forall T \le \bar{T}_{\mathrm{l}} \\ 1 & , \ \forall T > \bar{T}_{\mathrm{l}} \end{cases} \tag{6}$$

where $\bar{T}_{\mathrm{l}}$ and $\bar{T}_{\mathrm{s}}$ are the liquidus and solidus temperatures of the alloy respectively. In this non-isothermal phase-change case, the material viscosity in the mushy zone is governed by the Equation (4). The thermal and flow material properties are described in Table V. The resulting Rayleigh, Prandtl and Stefan numbers are 10^4, 10^3 and 5 respectively.

The finite element mesh used in the computations is the 50×50 mesh already considered in the first example. According to Reference [2], the time step chosen was 10.

Figure 11(a) shows the velocity field for $t = 1000$ and, additionally, the position and shape of the mushy region denoted by the solidus (-0.1) and liquidus (0.1) lines. The maximum velocity value is 0.011033. The solidus line presents a small deformation owing to the convection similar in shape to the deformation predicted in an isothermal phase-change case. The liquidus front, however, shows a pronounced curvature along the lower wall. This fact is

a direct effect of the convection in the mushy zone. The flow direction, away from the cold wall, increases the heat loss in the area and hence extends the mushy region. At the same time the return flow from the hot wall retards the growth of the mushy zone at the top of the cavity producing a great curvature at the bottom. The isotherms at $t = 1000$ are plotted in Figure 11(b). All these results are in overall good agreement with those obtained in Reference [2] using an enthalpy–porosity technique. Moreover, Figure 11(c) plots the position of the liquidus and solidus temperature lines obtained in the present work and those reported in Reference [2]. As may be seen, both results compare well and predict very similar mushy region location.

4.4. Solidification of an aluminium alloy with a wide phase-change interval

The analysis of the heat and flow behaviours of an aluminium alloy (Al–7%Si–0.3%Mg) during solidification is studied. The problem layout (geometry, initial and boundary conditions) is essentially the same as in the first example but now the solidifying material is an aluminium alloy with a large phase-change interval, i.e. $\bar{T}_l = 615°C$ and $\bar{T}_s = 545°C$. The corresponding phase-change function f_{pc} or liquid fraction based on experimental measurements is given in Figure 12 [33,34] and, consequently, it is used to define the viscosity according to Equation (4). The temperature-dependent thermal properties of the alloy are described in Table VI [34]. The density, dynamic viscosity and thermal dilatation coefficient are equal to those shown in Table I. The Rayleigh number considered is 10^4 and the transient analysis is carried out with a dimensionless time step of 0.01 using the 50×50 mesh of the first example.

The objective of this example is to analyse the flow behaviour and the heat transfer conditions for an alloy characterized with a more realistic phase-change function and thermal material properties. This function has been used in purely thermal analyses giving better predictions than those obtained with the more standard expressions, such as the linear or parabolic functions, the lever rule, the Scheil's equation, etc. [34].

The velocity and temperature fields at three different dimensionless times of the analysis are presented in Figure 13. The maximum dimensionless velocity values for these times are 0.1677, 0.1272 and 0.0347 respectively. As it can be seen, the convective effects do not play a significant role in the early stages of the process. From times equalling 30 and onwards, the growth of the mushy region at the bottom of the cavity is apparent leading to a large distortion in the liquidus front. For time $t = 90$, no liquid phase is present; however, the maximum velocity value in the rest of the mushy zone is only five times smaller than the maximum value during the whole process. The total dimensionless solidification time is 1.38.

Table V. Mushy region test problem data.

Conductivity (k)	0.001
Specific heat (c)	1.0
Latent heat (L)	5.0
Density (ρ)	1.0
Dynamic viscosity of the liquid phase (μ_l)	1.0
Thermal dilatation coefficient (α)	0.01
Solidus temperature ($\bar{T}_s$)	-0.1
Liquidus temperature ($\bar{T}_l$)	0.1

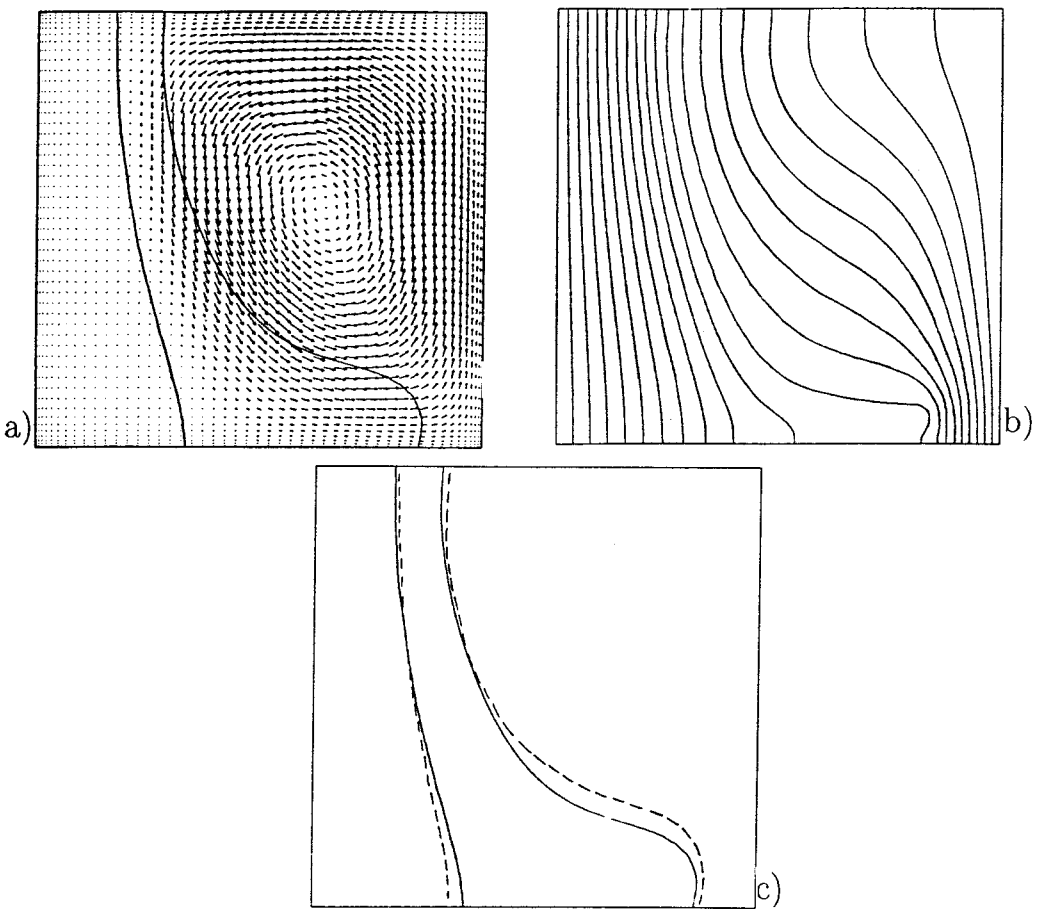

Figure 11. Mushy region test problem. Results at time 1000: (a) velocity field, (b) isotherms (0.05 apart) and (c) liquidus and solidus temperature lines location (– – –, Voller and Prakash [2]; and —, present work).

In order to compare the influence of the choice of f_{pc} on the velocity and temperature fields, a similar analysis has been performed with a phase-change function given by the lever rule

$$f_{pc} = \begin{cases} 0 & , \ \forall T \le \bar{T}_s \\ 0 < 1 - \dfrac{1}{(1-p)} \dfrac{T - \bar{T}_l}{T - \bar{T}_m} \le 1 & , \ \bar{T}_s < \forall T \le \bar{T}_l \\ 1 & , \ \forall T > \bar{T}_l \end{cases} \tag{7}$$

with $p = (\bar{T}_m - \bar{T}_l)/(\bar{T}_m - \bar{T}_s) = 0.3913$ being the partition coefficient and $\bar{T}_m$ the melting temperature of pure aluminium (660°C). The corresponding results are plotted in Figure 14. The maximum dimensionless velocity values for the times mentioned above are 0.1619, 0.1244 and 0.0318 respectively. Although these values are close to those related with the experimental f_{pc}, the mushy zone evolution is clearly different. In particular, the solidus and liquidus lines move slower when the lever rule is considered. This fact is also reflected in the solidification times, as the dimensionless solidification time in this last case is 1.52. For a given temperature, a smaller liquid fraction is normally obtained for the second case and, taking into account Equation (4), this explains the different behaviour between these two cases.

5. CONCLUSIONS

A finite element thermally coupled incompressible flow formulation including isothermal and non-isothermal phase-change effects has been presented. This proposed fixed-domain methodology, written in terms of the primitive variables of the problem (velocity, pressure and temperature), is defined in the context of the GSO technique and constitutes the main original contribution of this work. The resulting coupled system of equations is approached via an incremental iterative staggered scheme, which guarantees a fully coupled numerical solution in every time step of the analysis.

This formulation has been used in the analyses of a melting and solidification problems. The relevant features of this formulation have been explicitly detailed in these examples. In

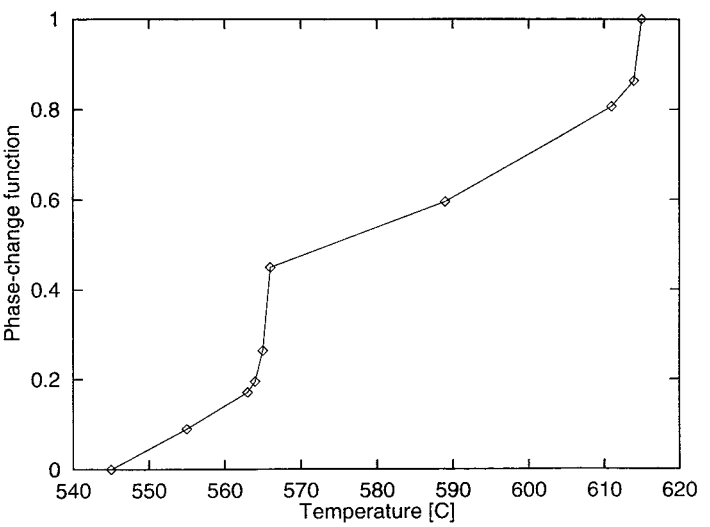

Figure 12. Solidification of an aluminium alloy with a wide phase-change interval. Phase-change function.

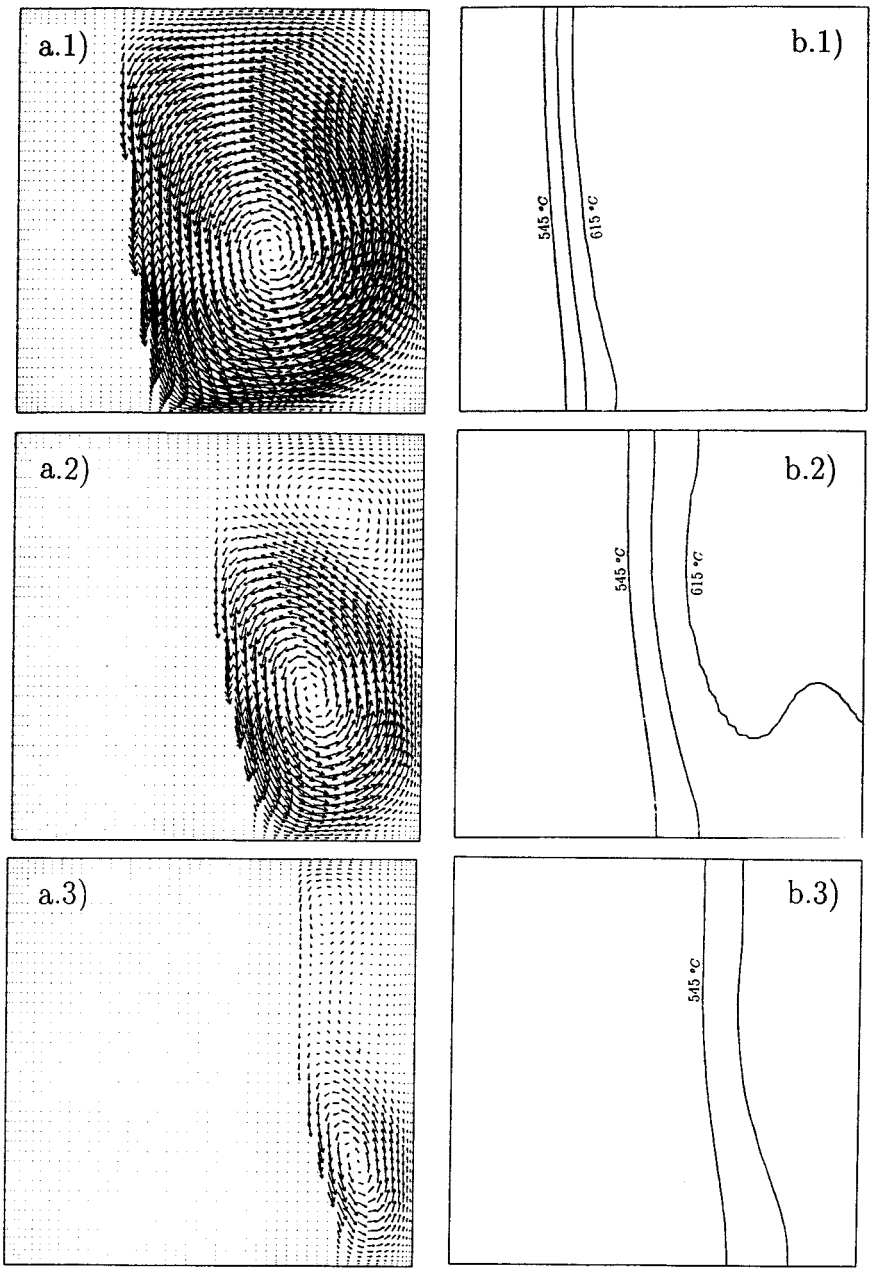

Figure 13. Solidification of an aluminium alloy with a wide phase-change interval. (a) Velocity field and (b) mushy zone isotherms for the experimental phase-change function at dimensionless times (1) 0.30, (2) 0.60 and (3) 0.90 (the isotherms are 35°C apart).

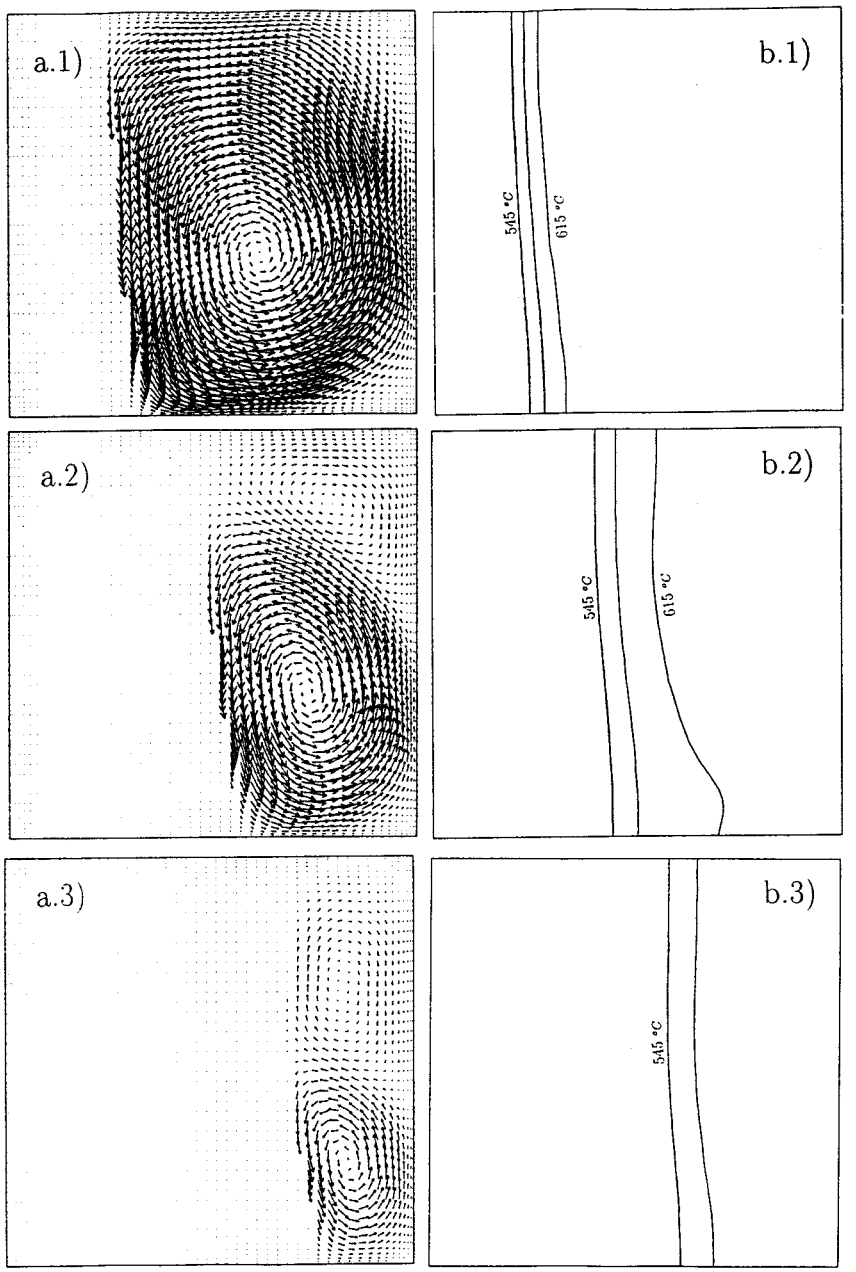

Figure 14. Solidification of an aluminium alloy with a wide phase-change interval. (a) Velocity field and (b) mushy zone isotherms for the lever rule at dimensionless times: (1) 0.30, (2) 0.60 and (3) 0.90 (the isotherms are 35°C apart).

Table VI. Thermal properties of an aluminium alloy.

Specific heat:	
c [J (kg K)$^{-1}$]	T (°C)
876	0
926	100
972	200
1017	300
1061	400
1105	500
1125	545
1125	555
1085	611
Conductivity:	
k [J (m s K)$^{-1}$]	T (°C)
160	0
150	100
140	400
150	555
134	568
116	570
98	603
95	608
100	611
200	620
300	650
500	750
Specific latent heat:	
$L \times 10^3$ (J kg^{-1})	T (°C)
495	545
495	564
398	565
398	615

The variations of c, k and L have been assumed to be piecewise linear within the mentioned temperatures. Below the lowest and above the highest temperatures, the properties are assumed to remain constant at the same value defined for the extreme temperature.

particular, in the solidification of pure aluminium in a square region, the influence of the flow pattern for different Rayleigh numbers over the phase-change front position has been studied. Characteristic parameters obtained in this work adjust properly with those reported in the literature. Moreover, numerical convergence has been also achieved for high Rayleigh numbers and acceptable results have been obtained with coarse meshes. In the second example, the

numerical results of the present formulation have been also compared with some laboratory measurements conducted on pure metal gallium and a numerical solution published by other author showing a satisfactory agreement between them. In these isothermal phase-change problems, an improved numerical integration procedure has been used to accurately compute the phase-change and viscosity terms. The last two examples deal with non-isothermal phase-change problems, where the mushy flow behaviour is particularly studied with a viscosity model valid for equiaxed metal solidification and written as a function of the liquid fraction. In the mushy region test problem, a good comparison with other numerical approach has been obtained. Finally, the solidification of an aluminium alloy with a wide phase-change interval has been analysed with an experimental-based phase-change function and these results have been compared with those computed using the lever rule. The different response demonstrated that the form of latent heat release is an important variable in the description of the flow behaviour.

ACKNOWLEDGMENTS

The financial support provided by FONDECYT Project No. 1980054 and DICYT/USACH Projects Nos. 01-9716Cr and 01-9716Ce are gratefully acknowledged.

REFERENCES

1. Voller V, Cross M, Markatos N. An enthalpy method for convection/diffusion phase change. *International Journal for Numerical Methods in Engineering* 1987; **24**: 271–284.
2. Voller V, Prakash C. A fixed grid numerical modelling methodology for convection–diffusion mushy region phase-change problems. *International Journal for Heat and Mass Transfer* 1987; **30**(8): 1709–1719.
3. Bennon W, Incropera F. A continuum model for momentum, heat and species transport in binary solid–liquid phase change systems—I. Model formulation. *International Journal for Heat and Mass Transfer* 1987; **30**(10): 2161–2170.
4. Brent A, Voller V, Reid K. Enthalpy–porosity technique for modelling convection–diffusion phase change. *Numerical Heat Transfer* 1988; **13**: 297–318.
5. Beckermann C, Viskanta R. Natural convection solid/liquid phase change in porous media. *International Journal for Heat and Mass Transfer* 1988; **31**(1): 35–46.
6. Voller V, Brent A, Prakash C. The modelling of heat, mass and solute transport in solidification systems. *International Journal for Heat and Mass Transfer* 1989; **32**(9): 1719–1731.
7. Swaminathan C, Voller V. On the enthalpy method. *International Journal for Numerical Methods in Heat and Fluid Flow* 1993; **3**: 233–244.
8. Krane M, Incropera F, Gaskell D. Solidification of ternary metal alloys—I. Model development. *International Journal for Heat and Mass Transfer* 1997; **40**(16): 3827–3835.
9. Krane M, Incropera F. Solidification of ternary metal alloys—II. Predictions of convective phenomena and solidification behavior in Pb–Sb–Sn alloys. *International Journal for Heat and Mass Transfer* 1997; **40**(16): 3837–3847.
10. Krane M, Incropera F. Experimental validation of continuum mixture model for binary alloy solidification. *Journal for Heat Transfer* 1997; **119**: 783–791.
11. Dantzig J. Modelling liquid–solid phase changes with melt convection. *International Journal for Numerical Methods in Engineering* 1989; **28**: 1769–1785.
12. Kim J, Lim I, Yang H, Meyers C. Comparison of four different latent heat models during the phase–change process. *AFS Transactions* 1992; **127**: 947–954.
13. Heinrich J, Felicelli S, Poirier D. Vertical solidification of dendritic binary alloys. *Computer Methods in Applied Mechanics and Engineering* 1991; **89**: 435–461.
14. Shirvanian A, Faghri M, Zhang Z. Numerical solution of the effect of vibration on melting of unfixed rectangular phase-change material under variable-gravity environment. *Numerical Heat Transfer*, *Part A: Applications* 1998; **34**(3): 257–278.

15. Simpson J, Garimella S. An investigation of the solutal, thermal and flow fields in unidirectional alloy solidification. *International Journal for Heat and Mass Transfer* 1998; **41**(16): 2485–2502.
16. Gong Z, Mujumdar A. Flow and heat transfer in convection-dominated melting in a rectangular cavity heated from below. *International Journal for Heat and Mass Transfer* 1998; **41**(17): 2573–2580.
17. Huang H, Usmani A. *Finite Element Analysis for Heat Transfer: Theory and Software*. Springer: London, 1994.
18. Jaisuk Y, Rubinsky R. A finite element method for the study of solidification processes in the presence of natural convection. *International Journal for Numerical Methods in Engineering* 1986; **23**: 1785–1805.
19. McDaniel D, Zabaras N. A least-squares front-tracking finite element method analysis of phase-change with natural convection. *International Journal for Numerical Methods in Engineering* 1994; **37**: 2755–2777.
20. Zabaras N, Nguyen T. Control of the freezing interface morphology in solidification processes in the presence of natural convection. *International Journal for Numerical Methods in Engineering* 1995; **38**: 1555–1578.
21. Yang G, Zabaras N. An adjoint method for the inverse design of solidification processes with natural convection. *International Journal for Numerical Methods in Engineering* 1998; **42**: 1121–1144.
22. Cruchaga M, Oñate E. A finite element formulation for incompressible flow problems using a generalized streamline operator. *Computer Methods in Applied Mechanics and Engineering* 1997; **143**: 49–67.
23. Cruchaga M. A study of the backward-facing step problem using a generalized streamline formulation. *Communications in Numerical Methods in Engineering* 1998; **14**: 697–708.
24. Hughes TJR, Mallet M. A new finite element formulation for computational fluid dynamics: III. The generalized streamline operator for multidimensional advective–diffusive systems. *Computer Methods in Applied Mechanics and Engineering* 1986; **58**: 305–328.
25. Hughes TJR, Franca LP, Ballestra M. A new finite element formulation for computational fluid dynamics: V. Circumventing the Babuska–Brezzi condition: a stable Petrov–Galerkin formulation of the Stokes problem accommodating equal-order interpolations. *Computer Methods in Applied Mechanics and Engineering* 1986; **59**: 85–99.
26. Barbosa HJ, Hughes TJR. Circumventing the Babuska–Brezzi condition in mixed finite element approximations of elliptic variational inequalities. *Computer Methods in Applied Mechanics and Engineering* 1992; **97**: 193–210.
27. Celentano D, Oñate E, Oller S. A temperature-based formulation for finite element analysis of generalized phase-change problems. *International Journal for Numerical Methods in Engineering* 1994; **37**: 3441–3465.
28. Celentano D, Pérez E. A phase-change formulation including general latent heat effects. *International Journal for Numerical Methods in Heat and Fluid Flow* 1996; **6**(8): 71–79.
29. Celentano D. A finite element formulation for phase-change problems with advective effects. *Communications in Numerical Methods in Engineering* 1998; **14**: 719–730.
30. Cruchaga M, Celentano D. A thermally coupled incompressible flow formulation with phase-change effects. Proceedings of the Tenth International Conference on Numerical Methods for Thermal Problems, Swansea, U.K, 1997.
31. Zienkiewicz OC, Taylor RL. *The Finite Element Method* (4th edn). McGraw-Hill: New York, 1989.
32. Gau C, Viskanta R. Melting and solidification of a pure metal on a vertical wall. *Journal of Heat Transfer* 1986; **108**: 171–174.
33. Tamminen J. Thermal analysis for investigation of solidification mechanisms in metal and alloys. PhD thesis, University of Stockholm, Sweden, 1988.
34. Gunasegaram D, Celentano D, Nguyen T. The effect of cooling a permanent composite mold on air gap formation and heat transfer. In *Proceedings of the 126th TMS Annual Meeting & Exhibition*, Viswanathan S, Reddy RG, Malas JC (eds). TMS (The Minerals, Metals and Materials Society): Orlando, U.S.A., 1997; 101–116.

